NeuroImage 276 (2023) 120202

Contents lists available at ScienceDirect

NeuroImage

journal homepage: www.elsevier.com/locate/neuroimage

High angular resolution susceptibility imaging and estimation of fiber orientation distribution functions in primate brain

Dimitrios G. Gkotsoulias[a,*], Roland Müller[a], Carsten Jäger[b], Torsten Schlumm[a], Toralf Mildner[a], Cornelius Eichner[c], André Pampel[a], Jennifer Jaffe[d,e], Tobias Gräßle[e,f,g], Niklas Alsleben[b], Jingjia Chen[h], Catherine Crockford[d,e,i], Roman Wittig[d,e,i], Chunlei Liu[h,j], Harald E. Möller[a]

[a] Nuclear Magnetic Resonance Methods & Development Group, Max Planck Institute for Human Cognitive and Brain Sciences, Leipzig, Germany
[b] Department of Neurophysics, Max Planck Institute for Human Cognitive and Brain Sciences, Leipzig, Germany
[c] Department of Neuropsychology, Max Planck Institute for Human Cognitive and Brain Sciences, Leipzig, Germany
[d] Max Planck Institute for Evolutionary Anthropology, Leipzig, Germany
[e] Taï Chimpanzee Project, Centre Suisse de Recherches Scientifiques en Côte d'Ivoire, Côte d'Ivoire
[f] Helmholtz Institute for One Health, Greifswald, Germany
[g] Robert Koch Institute, Epidemiology of Highly Pathogenic Microorganisms, Berlin, Germany
[h] Electrical Engineering and Computer Sciences, University of California, Berkeley, CA, USA
[i] Institute of Cognitive Sciences, CNRS UMR5229 University of Lyon, Bron, France
[j] Helen Wills Neuroscience Institute, University of California, Berkeley, CA, USA

ARTICLE INFO

Keywords:
Anisotropic magnetic susceptibility
Diffusion-weighted imaging
Gradient-recalled echo
High angular resolution
Orientation distribution function, Quantitative susceptibility mapping

ABSTRACT

Uncovering brain-tissue microstructure including axonal characteristics is a major neuroimaging research focus. Within this scope, anisotropic properties of magnetic susceptibility in white matter have been successfully employed to estimate primary axonal trajectories using mono-tensorial models. However, anisotropic susceptibility has not yet been considered for modeling more complex fiber structures within a voxel, such as intersecting bundles, or an estimation of orientation distribution functions (ODFs). This information is routinely obtained by high angular resolution *diffusion* imaging (HARDI) techniques. In applications to fixed tissue, however, diffusion-weighted imaging suffers from an inherently low signal-to-noise ratio and limited spatial resolution, leading to high demands on the performance of the gradient system in order to mitigate these limitations. In the current work, high angular resolution *susceptibility* imaging (HARSI) is proposed as a novel, phase-based methodology to estimate ODFs. A multiple gradient-echo dataset was acquired in an entire fixed chimpanzee brain at 61 orientations by reorienting the specimen in the magnetic field. The constant solid angle method was adapted for estimating phase-based ODFs. HARDI data were also acquired for comparison. HARSI yielded information on whole-brain fiber architecture, including identification of peaks of multiple bundles that resembled features of the HARDI results. Distinct differences between both methods suggest that susceptibility properties may offer complementary microstructural information. These proof-of-concept results indicate a potential to study the axonal organization in *post-mortem* primate and human brain at high resolution.

Abbreviations: 3D, three-dimensional; CAD, computer aided design; CITES, Convention on International Trade in Endangered Species of Wild Fauna and Flora; CSA, constant solid angle; DTI, diffusion tensor imaging; DWI, diffusion-weighted imaging; EPI, echo planar imaging; ESPIRiT, iTerative Eigenvector-based Self-consistent Parallel Imaging Reconstruction; FDT, FMRIB Diffusion Toolbox; FLASH, Fast Low-Angle SHot; FLIRT, FMRIB's Linear Image Registration Tool; FSL, FMRIB Software Library; GM, gray matter; GRAPPA, GeneRalized Autocalibrating Partially Parallel Acquisitions; GRE, gradient-recalled echo; HARDI, high angular resolution diffusion imaging; HARSI, high angular resolution susceptibility imaging; iLSQR, iterative LSQR; LSQR; ME, multi echo; MLE, maximum likelihood estimation; MRI, magnetic resonance imaging; MP2RAGE, Magnetization-Prepared 2 RApid Gradient Echoes; NMI, normalized mutual information; ODF, orientation distribution function; PBS, phosphate-buffered saline; PE, phase-encoding; PFA, paraformaldehyde; QSM, quantitative susceptibility mapping; RF, radiofrequency; ROI, region of interest; SSIM, structural similarity index measure; STI, susceptibility tensor imaging; STL, stereolithography; SVD, singular value decomposition; V-SHARP, Variable-kernel Sophisticated Harmonic Artifact Reduction for Phase data; WM, white matter.

* Corresponding author at: Max Planck Institute for Human Cognitive and Brain Sciences, Stephanstraße 1A, 04103 Leipzig, Germany.
E-mail address: gkotsoulias@cbs.mpg.de (D.G. Gkotsoulias).

https://doi.org/10.1016/j.neuroimage.2023.120202.
Received 19 October 2022; Received in revised form 21 May 2023; Accepted 27 May 2023
Available online 27 May 2023.
1053-8119/© 2023 Published by Elsevier Inc. This is an open access article under the CC BY-NC-ND license (http://creativecommons.org/licenses/by-nc-nd/4.0/)

Mathematical symbols

δB_0:	local offset of the amplitude of the magnetic flux density;
BW:	bandwidth;
b:	b-value;
FA:	fractional anisotropy;
FOV:	field of view;
f_p:	partial-Fourier factor;
H_0:	magnitude of the applied magnetic field;
$\hat{\mathbf{H}}$:	unit vector along the direction of the applied magnetic field;
$\mathbf{k}$:	spatial frequency vector;
MD:	mean diffusivity;
MMS:	mean magnetic susceptibility;
MSA:	magnetic susceptibility anisotropy;
n:	number (integer);
R:	GRAPPA acceleration factor;
R_2^*:	effective transverse relaxation rate;
$\mathbf{r}$:	position vector;
SD:	standard deviation;
SNR:	signal-to-noise ratio;
T_1:	longitudinal relaxation time;
TA:	acquisition time;
TE:	echo time;
ΔTE:	echo spacing;
TR:	repetition time;
x, y, z:	cartesian coordinates;
α:	RF pulse flip angle,
γ:	gyromagnetic ratio;
φ:	signal phase;
$\lambda_1, \lambda_2, \lambda_3$:	eigenvalues of the diffusion tensor;
μ_0:	vacuum permeability;
χ:	bulk volume magnetic susceptibility;
$\boldsymbol{\chi}$	magnetic susceptibility tensor;
χ_1, χ_2, χ_3:	eigenvalues of the magnetic susceptibility tensor;
χ_{ij}:	magnetic susceptibility tensor element;
$\mathcal{F}$, $\mathcal{F}^{-1}$:	Fourier transform and inverse Fourier transform;
^{T}:	transpose of a matrix.

1. Introduction

Volume magnetic susceptibility (χ) is a dimensionless quantity (in SI units), which describes the degree of magnetization of a material placed inside an external magnetic field. In biological tissues, local structural characteristics lead to spatial variations of susceptibility and, thus, to local field disturbances and measurable differences in the resonance frequency in magnetic resonance imaging (MRI). Based on the nature of these disturbances, susceptibility may be paramagnetic ($\chi > 0$) or diamagnetic ($\chi < 0$). In reverse, quantifying the susceptibility properties of tissue can lead to a non-invasive elucidation of microstructural properties and details at the whole-brain scale, without the need for sophisticated microscopy techniques (Möller et al., 2019).

Quantitative susceptibility mapping (QSM) methods provide voxel-wise susceptibility estimations based on the signal phase in gradient-recalled echo (GRE) acquisitions and a series of post-processing steps (Deistung et al., 2017; de Rochefort et al., 2010; Liu et al., 2015; Shmueli et al., 2009). Although various approaches have been developed for this purpose, robust mapping of χ from MRI phase data remains challenging because the field perturbation (and, hence, the signal phase) associated with a susceptibility distribution is inherently non-local and depends on the distribution's orientation in the magnet (Schäfer et al., 2009). Briefly, following appropriate combination of the complex multi-channel data from a phased-array coil and removal of phase wraps (Robinson et al., 2017) and background-field contributions (Schweser et al., 2017), field-to-source inversion methods are used to solve (in the Fourier domain) the ill-posed problem of going from the signal phase (as a measure of the local magnetic flux density offset, δB_0) to the local variations in χ. Notably, this is typically performed under the assumption that χ representing an imaging voxel is a scalar, isotropic quantity (Deistung et al., 2017). While this assumption may be justified in regions of cerebral gray matter (GM), multiple studies have shown that the bulk susceptibility in cerebral white matter (WM) exhibits a highly anisotropic character—primarily, as a result of the specific arrangement of the myelin sheaths enveloping axons at a molecular level, leading to an accumulated macroscopic effect on the voxel level (Li et al., 2017; Liu, 2010; Wharton & Bowtell, 2012).

Consequently, brain tissue susceptibility cannot be fully understood and exploited if its anisotropic characteristics are not taken into consideration—similarly to diffusion tensor imaging (DTI) that exploits the anisotropic characteristics of diffusion as an expansion of simple measurements of the mean diffusivity (MD). Methods proposed for addressing this issue, such as susceptibility tensor imaging (STI), consider multiple GRE acquisitions by reorienting the object (e.g., the human head) inside the magnet—as current MRI technology does not allow to reorient the magnetic field around the imaged object (Liu, 2010). In the basic STI approach, susceptibility is depicted as a second-rank symmetric tensor with six unique parameters, in a similar way as orientation-dependent diffusivity is modeled in DTI (Basser et al., 1994a; 1994b). Obtaining GRE phase measurements along six or more unique orientations allows for the reconstruction of a second-rank tensor $\boldsymbol{\chi}$, based on a linear system of equations constructed by the relationship (Li et al., 2017; Liu, 2010):

$$\delta B_0(\mathbf{r}) = \frac{\varphi(\mathbf{r}, \mathrm{TE})}{2\pi\gamma \cdot \mathrm{TE}} = \mu_0 H_0 \cdot \mathcal{F}^{-1}\left[\frac{1}{3}\hat{\mathbf{H}}^T\ \mathcal{F}(\boldsymbol{\chi})\ \hat{\mathbf{H}} - \hat{\mathbf{H}} \cdot \mathbf{k}\frac{\mathbf{k}^T\ \mathcal{F}(\boldsymbol{\chi})\ \mathbf{H}}{k^2}\right], \quad (1)$$

In Eq. (1), $\varphi(\mathbf{r}, \mathrm{TE})$ is the signal phase in image space at position $\mathbf{r}$ and echo time TE, γ is the gyromagnetic ratio, μ_0 is the vacuum permeability, H_0 and $\hat{\mathbf{H}}$ are, respectively, the magnitude of the applied magnetic field and its unit vector (defining the laboratory frame's z-direction), and $\mathbf{k}$ is the spatial frequency vector. $\mathcal{F}$ and $\mathcal{F}^{-1}$ denote the Fourier transform and its inverse, respectively, and the subscript ^{T} the transpose. Note that the χ_{33} tensor component has also been suggested as an STI-based estimation of a scalar susceptibility (Langkammer et al., 2018).

Despite being a useful approximation of the diffusion signal for a certain range of b-values (Novikov et al., 2018), DTI is mathematically incapable of resolving multiple fiber orientations within a voxel, thus providing limited information for the vast majority of WM regions (Jones et al., 2013). Important improvements are achieved with High Angular Resolution Diffusion Imaging (HARDI) techniques, sampling 60 or even more diffusion directions (Frank et al., 2001; Tournier et al., 2004; Tuch et al., 2002; 1999). This includes high-quality estimations of fiber orientation distribution functions (ODFs) and resolving intersecting fiber bundles. Compared to these developments in diffusion-weighted imaging (DWI), the need for physical rotation of the object and the complex processing pipeline of multi-orientational susceptibility imaging has led to datasets of limited angular resolution so far. For example, STI acquisitions in formalin-fixed mouse brain specimens were obtained with 19 orientations, which were evenly distributed on a spherical surface if a sufficiently large radiofrequency (RF) coil could be used (Liu et al., 2012) but restricted to rotations about the sample's long axis with a tightly fitting solenoid (Li et al., 2012a). *In-vivo* acquisitions in humans achieved 12–17 rotation angles (about the anterior-posterior and the left-right direction) varying between ±25° and ±50° depending on the spatial constrictions imposed by the employed head coil (Bilgic et al., 2016a; Li et al., 2012a; Shi et al., 2022). Such constraints impose limitations on the quality of tensor-based analyses and, more importantly, prohibit to go beyond STI for microstructural information, such as susceptibility-based ODFs (Liu et al., 2013).

In the current work, we introduce High Angular Resolution Susceptibility Imaging (HARSI) as an advanced QSM approach for *post-mortem* acquisitions—similar to HARDI techniques developed in the context of DWI. The goal is to investigate the orientation-dependent susceptibility at high angular resolution to achieve WM characterization beyond state-of-the-art tensor-based methods. A multi-echo (ME) GRE dataset comprising 61 unique directions is presented, and HARSI-based STI estimates are compared to single-orientation QSM results. Additionally, ODFs are obtained by applying the generalized constant solid angle (CSA) method (Kamath et al., 2012). The results indicate comparable potential in resolving intersecting fiber orientations as HARDI-based ODFs and suggest strong prospects for obtaining complementary information on WM microstructure.

2. Methods

2.1. Brain specimen

The *post-mortem* specimen used for the acquisitions was a whole brain obtained from an adult wild alpha-male chimpanzee (*Pan troglodytes verus*; male, 45 years). The animal had died from natural causes in Taï National Park (Parc National de Taï), Côte d'Ivoire, without human interference. Approximately 18 h after death, a specifically trained veterinarian performed the brain extraction wearing full personal protective equipment and adhering to the necroscopy protocols at the field site. All procedures followed the ethical guidelines of primatological research at the Max Planck Institute for Evolutionary Anthropology, Leipzig, which were approved by the Ethics Committee of the Max Planck Society. Immediately after extraction, the brain was preserved by immersion in 4% paraformaldehyde (PFA). The specimen was transferred to Germany under strict observation of CITES (Convention on International Trade in Endangered Species of Wild Fauna and Flora) protocol regulations. After fixation for 6 months, superficial blood vessels were removed, and the PFA was washed out in phosphate-buffered saline (PBS) at pH 7.4 for 24 days.

2.2. Brain container for reorientation imaging

For preparatory experiments, the specimen was centered in an oval-shaped acrylic container of suitable size (15cm long-axis and 10cm short-axis diameter) and stabilized with sponges. The container was filled with liquid perfluoropolyether (Fomblin®; Solvay Solexis, Bollate, Italy) to protect the tissue from dehydration and to achieve approximate matching of the susceptibility at the brain surface (Benveniste et al., 1999). With this setup, a three-dimensional (3D) high-resolution T_1-weighted MP2RAGE (Magnetization-Prepared 2 RApid Gradient Echoes) dataset was acquired.

Phase-sensitive acquisitions at multiple orientations with respect to the main magnetic field require physical rotations of the object. During these measurements, the sample may be subjected to gravity-induced non-linear deformations, which are inconsistent between scans unless measures are taken to preserve the shape. This leads to inaccuracies and may introduce artifacts during post-processing, which requires excellent registration of the acquired volumes. In previous *post-mortem* experiments in mice (Li et al., 2012a; Liu et al., 2012) and also in humans (Alkemade et al., 2020; 2022), the problem of inconsistent deformations was avoided by keeping the fixed brain within the skull after surgical separation of the head. In the current work, a specific brain mask was derived from the 3D T_1-weighted dataset and a custom-made container was designed consisting of an inner and an outer part (Fig. 1B–E). Based on the mask, the surface of the individual anatomy was reconstructed and split into a top and a bottom mesh using Python (Fig. 1B). The algorithm further allowed for a parameterization of the design, for example, to consider an additional distance from the tissue or modify the wall thickness for sufficient stability. Stereolithography (STL) files were then produced using CAD (computer-aided design) software (Fusion 360®; Autodesk, San Rafael, CA, USA). The outer container was a spherical structure of sufficient size (16cm diameter) to take up the anatomically shaped inner container, which was rigidly connected via eight adjustable screws (Fig. 1E). The spherical outer shell also consisted of two parts (top and bottom) with further indications of 60 unique orientations on its surface (Fig. 1B and Supplementary Figure S1). The orientations were calculated employing an electrostatic repulsion optimization model using *MRtrix3* (Jones et al., 1999; Tournier et al., 2019). The outer container was then positioned on a custom-made holder that included an additional position indicator (Fig. 1E). The combined setup ensured robust positioning of the specimen in the RF coil with an orientation error $\leq 3^{\circ}$ for all axes. Note that refined orientation information was obtained during post-processing from image registration (see below) and used in all subsequent analyses. All container and holder parts were 3D-printed on an Objet Eden260VS (Stratasys, Eden Prairie, MN, USA) using Objet MED610 Biocompatible Clear material (Stratasys). Preliminary tests indicated no visible artifacts or distortions related to the material and its interface with the tissue or Fomblin, which was also confirmed in experiments at higher magnetic field (7 T).

Special care is required to thoroughly remove bubbles that may form when the specimen is placed in the individualized container. The brain, initially stored in PBS, was taken out of the aqueous medium, placed on a soft tissue to remove dripping PBS and submerged in Fomblin. Deeper localized air bubbles and aqueous residues were removed from the specimen under low vacuum. The brain was placed in the bottom part of the inner container and stabilized with flat sponges (if necessary). The container was closed with the top part, tightened with polytetrafluoroethylene tape (Teflon™; Chemours Deutschland, Neu-Isenburg, Germany) and sealed carefully with Temflex™ vinyl tape (3M Deutschland, Neuss, Germany). Fomblin that had been degassed under vacuum was added through holes in the top part (Fig. 1B and Supplementary Figure S1), which were temporarily sealed with Temflex tape. Subsequently, the container was placed on a laboratory shaker for some hours to help air bubbles rise to the surface. The procedure of adding degassed Fomblin, sealing and shaking was repeated several times, with different orientations of the container on the shaker. Before final sealing, a GRE-scan was performed to verify the removal of the majority of air bubbles. Finally, the sealed inner container was mounted in the outer container (Supplementary Figure S1).

2.3. Image acquisition

All MRI experiments were performed at 3 T on a MAGNETOM Skyra Connectom A (Siemens Healthineers, Erlangen, Germany) that achieves a maximum gradient strength of 300 mT/m (Fan et al., 2022). In order to avoid damage to the gradient coil during long scanning sessions, a first-order approximation of the acoustic response was computed in Matlab from the simulated gradient time course (IDEA DSV file) of each individual imaging protocol with its specific acquisition parameters (Labadie et al., 2013) and carefully inspected for potentially harmful vibrations. Before the scanning session, the specimen (within the container) was left in the scanner room to equilibrate with the room temperature. The brain container and holder were then positioned inside a 32-channel receive array coil (Siemens Healthineers), and a complex-valued 3D Fast Low-Angle SHot (FLASH) reference dataset (Frahm et al., 1986) was acquired after shimming. In particular, the specimen's long axis [i.e., anterior-posterior (AP) direction] was aligned with the magnet's y-axis and its left-right (LR) and superior-inferior (SI) directions with the magnet's x- and z-axes, respectively. In the following, this orientation is referred to as 'STI reference'. Subsequently, 60 additional consecutive acquisitions were performed with varying sample orientations and the same parameters as in the reference scan (1mm isotropic nominal resolution; field of view, FOV = 160 × 160 × 160 mm; RF pulse flip angle, $\alpha = 30°$; repetition time, TR = 50 ms; 12 echoes with TE = 3.54 ms and 6.98 ms for the first two echoes and an echo spacing, ΔTE = 3.75 ms, for the remaining 10

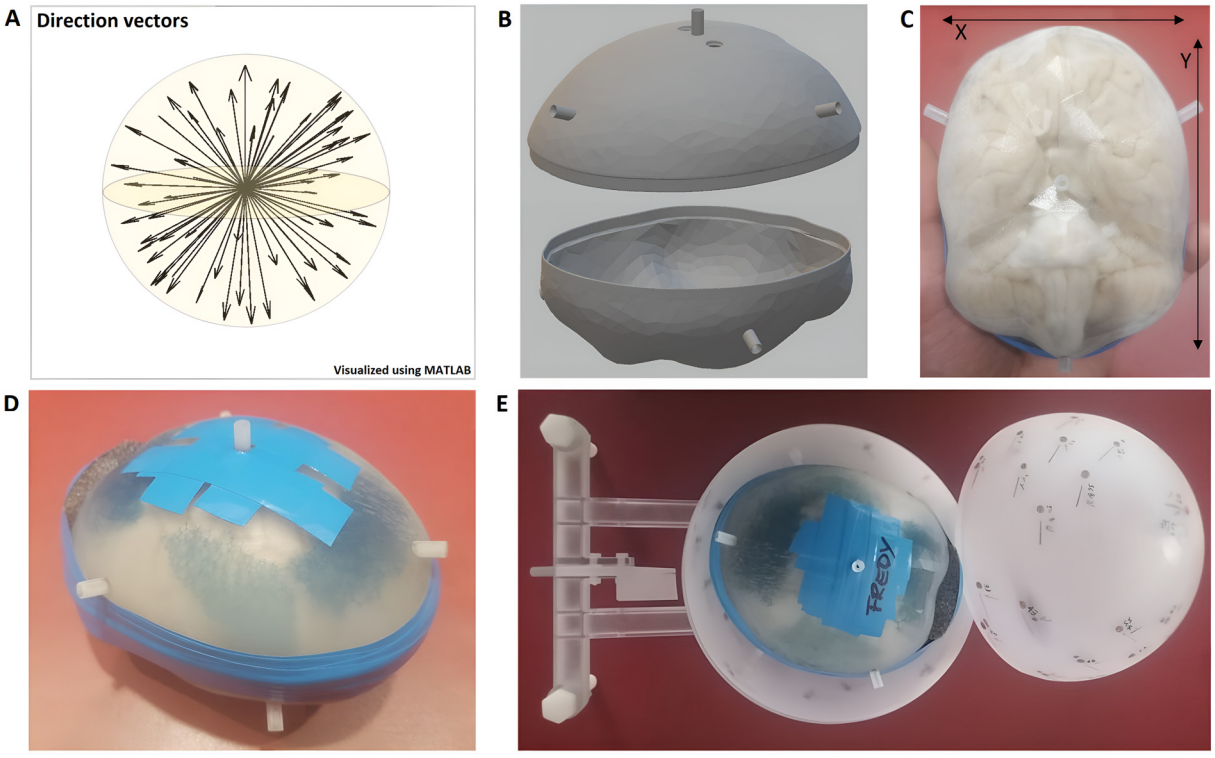

Fig. 1. **(A)** Direction unit vectors of 61 evenly distributed orientations on the surface of a sphere as calculated by *MRtrix3*. **(B)** Design of the inner container based on the surface rendering of a 3D T_1-weighted dataset. **(C, D)** 3D-printed container, adapted to the brain's individual anatomy with indications of the approximate dimensions. The specimen is immersed in Fomblin, and the container is carefully sealed using tape (x=105mm, y=125mm). **(E)** View of the specimen "Fredy" inside the anatomical container, positioned inside an outer, spherical container with indications of the calculated directions for reorientations. The outer container is positioned on a custom-made holder with an additional angle indicator that supports robust positioning in the RF coil and accurate reorientation.

echoes; bandwidth, BW = 600 Hz/pixel). GeneRalized Autocalibrating Partially Parallel Acquisitions (GRAPPA) with acceleration factor $R = 2$ (Griswold et al., 2002) and a partial-Fourier scheme (Feinberg et al., 1986) with partial-Fourier factor, $f_p = 7/8$ were employed in phase-encoding (PE) direction (along the z-axis of the laboratory frame), to accelerate the measurements (acquisition time, TA ≈ 12 min per orientation; total TA ≈ 12 : 12 h). The slab orientation was always along the magnet's y-axis (i.e., slices of the xz-plane in the laboratory frame or the typical coronal orientation for *in-vivo* brain MRI), and the vendor's 3D distortion correction was applied to all acquisitions. Temperature changes are known to affect susceptibility measurements (Birkl et al., 2015). To mitigate temperature drifts due to the energy deposited in the sample by repeated application of RF pulses, the orientation-dependent GRE scans were performed in batches of 4–5 acquisitions with a pause of approx. 30 min after each batch. Additional auxiliary experiments confirmed that this achieved stable temperature conditions within less than ±1 °C (see also Supplementary Figures S2 and S3).

Additional DWI data were acquired at 1mm isotropic nominal resolution with a previously described 3D segmented ME echo planar imaging (EPI) technique optimized for PFA-fixed tissue (Eichner et al., 2020). Briefly, the sequence consists of a Stejskal-Tanner sequence with multiple gradient-echo refocusing of the first (spin) echo. Combination of the GREs employing maximum likelihood estimation (MLE) yields a time-efficient increase of the signal-to-noise ratio (SNR) and reduced noise bias. Further acquisition parameters included FOV = 128 × 126 × 104 mm^3, TR = 10.4 s; TE = [53.5, 66, 78.5, 91] ms, BW = 1116 Hz/pixel, coronal orientation, foot-head PE direction, 18 segments, 1.14ms echo spacing. The specimen's AP direction was aligned to the magnet's z-axis in these scans. Sixty unique directions of the diffusion-weighting gradient were acquired with $b = 5000$ s/mm^2 in six batches of 10 scans and interleaved with seven acquisitions with $b = 0$ (TA ≈ 36 h). After each batch (i.e., roughly every 6 h), scanning was paused for approximately 1 h to mitigate heating of the specimen during the scanning session (Marschner et al., 2023).

2.4. Image processing

The complex-valued GRE data from each coil channel ($n = 32$) were saved individually for each orientation and the channel combination (with preservation of the phase information) was performed offline, based on singular value decomposition (SVD) and ESPIRiT (iTerative Eigenvector-based Self-consistent Parallel Imaging Reconstruction) (Bilgic et al., 2016b; Metere & Möller, 2017; Uecker et al., 2021; Uecker & Lustig, 2017). The multi-orientation phase volumes were registered to the 'STI reference' orientation to ensures that the calculated 3rd diagonal tensor element provides a good approximation for a scalar susceptibility estimate (Li et al., 2012b; Milovic et al., 2020). The required transformations were derived from registrations of the corresponding magnitude volumes using FSL-FLIRT (FSL 5.0.9) (Jenkinson et al., 2012) with 6-parameter rigid transformations, a normalized mutual information (NMI) cost function, and spline interpolation. The registration results were verified visually (Supplementary Figure S4) and, separately, based on the registration metrics from corresponding magnitude images (Supplementary Figure S5). The phase data from the acquisition at TE = 29.48 ms was selected for multi-orientation QS, which guaranteed enough phase evolution while still yielding sufficient SNR and a high contrast between GM and WM. We note that an increased SNR would be expected from integrating echo combination (Wu et al., 2012), which was not employed in the current work. Phase unwrapping was performed on the registered phase volumes using the Laplacian method (Schofield & Zhu, 2003), background-field removal using V-SHARP (Variable-kernel Sophisticated Harmonic Artifact Reduction for Phase

data) (Li et al., 2011; Özbay et al, 2017; Schweser et al., 2011), and field-to-source inversion, individually for all orientations, using an iterative LSQR solver in Matlab (iLSQR) (Li et al., 2011; 2015). The iLSQR algorithm as implemented in the STI Suite (Li et al, 2014) was also employed for susceptibility-tensor reconstruction and a decomposition into its eigenvalues (χ_1, χ_2, χ_3) and corresponding eigenvectors. Additionally, the previously introduced mean magnetic susceptibility (MMS) and magnetic susceptibility anisotropy (MSA) were calculated as orientation-independent tensor measures (Li et al., 2017). Separately, corresponding diffusion tensor reconstructions from the DWI data as well as calculations of eigenvalues (λ_1, λ_2, λ_3), eigenvectors, MD and fractional anisotropy (FA) were performed using the DTIFIT tool of the FMRIB Diffusion Toolbox (FDT; FSL 5.0.9).

Following registration of the GRE and DWI acquisitions to the same reference, voxel-wise CSA-ODFs were estimated separately from the orientation-dependent phase or diffusivity data using the DIPY package (Python). The DTI-based FA metric was employed for deriving a mask including only regions of sufficient tissue anisotropy (FA > 0.2). Further processing of the local phase data included outlier exclusion by thresholding and voxel-wise normalization to [0, 1] prior to the ODF estimation (Fig. 2).

For quality assessment, the SNR was calculated for each registered GRE volume based on the magnitude images. Briefly, GM and WM masks were calculated using thresholding on the reference GRE dataset, and a 3D region of interest (ROI) was defined within ranges of ±20 voxels in AP direction (as defined according to the brain sample; see Supplementary Figure S6), ±50 voxels in SI direction and ±25 voxels in right-left (RL) direction around the center (Fig. 3A–C). The ROI included the most significant WM areas as well as the cortical and subcortical GM. After isolating the ROI and masking, all remaining voxels were included in the analysis. Finally, an ROI of 30 × 30 × 30 voxels was identified within the artifact-free background to assess the noise, and simplified SNR estimates in GM and WM were obtained from the average signal intensities in the tissue segment divided by the standard deviation (SD) of the noise.

3. Results

3.1. Data quality

The image quality of the ME-GRE acquisitions at different orientations is demonstrated in Fig. 4A. Visual assessment of the local (tissue) phase of the reference volume for identifying artifacts indicated the presence of multiple small air bubbles within the cavity of the left lateral ventricle as well as single bubbles in two other regions (Fig. 4B). This verified that the bubble-removal procedure was successful in most parts of the specimen and that remaining artifacts did not degrade the data quality in regions selected for the further analysis. Due to the use of the close-fitting anatomically shaped container, FSL-FLIRT achieved consistent registrations to the reference of both the orientation-dependent GRE data as well as the DWI data. Maximum deviations in the SNR of the orientation-dependent GRE acquisitions were within ±8.4% compared to the reference result indicating consistent quality throughout the experiment (mean SNR ± SD: 33.0±1.1, range: 30.9–35.8 in GM and mean SNR ± SD: 22.5±0.8, range: 20.9–23.9 in WM). Fig. 3D further indicates an approximately linear decay of the SNR in both segments as a function of time. This decay during more than 12h scan time is of similar magnitude as the scan-to-scan SNR fluctuations and probably related to subtle drifts of the main field and shim currents. As such drift effects are corrected by the background-field removal of the QSM pipeline, they do not lead to a relevant degradation of the phase data. Visual inspection of the DWI data (Fig. 4C) indicates that an excellent quality is achieved with the segmented ME sequence implementation and the Connectom gradients, despite the substantially reduced diffusivity in fixed tissue at room temperature.

3.2. Tensor-based analyses

The high-angular GRE phase dataset provided unprecedented susceptibility tensor quality (Fig. 5A). Similarly, an excellent diffusion-tensor quality was obtained with DWI, which was of equivalent spatial and angular resolution as the GRE acquisitions (Fig. 5B). Consistently, the eigen-analysis of the diffusion data yielded a high quality of the MD and FA. The corresponding susceptibility metrics, MMS and MSA, yielded robust differentiation between WM and GM. The MMS exhibited local differences also within WM, indicating a particular sensitivity to the underlying microstructure of the voxels. The MSA results suggested a high sensitivity to microstructural changes but also to spurious noise from residual artifacts. Due to this slightly enhanced noise sensitivity of MSA, the DTI-derived FA map was selected as a more robust indicator of anisotropy.

The similarity of features extracted within WM with STI and DTI as indicated by a comparison of the color-coded primary eigenvectors in Fig. 5 (weighted by the FA for better visualization) is consistent with previous results employing a more restricted variation of orientations (Li et al., 2017). Note that the limitations inherent to mono-tensorial approaches allow for the identification of only a single maximum per voxel, corresponding to an average main fiber direction. Given this limitation, a qualitative resemblance of the STI and DTI results is obvious. Absolute similarity may not be expected due to the multi-step post-processing pipeline required for STI as well as contributions to susceptibility from other sources (e.g., iron) besides myelinated axons and differential sensitivities to fiber crossing between STI and DTI.

3.3. Impact from anisotropy in QSM

QSM results obtained assuming scalar isotropic susceptibility with eight sample orientations selected as examples (of the total of 61 acquisitions) are compared to the STI-derived ‘scalar’ susceptibility reference (i.e., the χ_{33} tensor component) in Fig. 6A. Visual inspection reveals obvious differences between acquisitions taken with different orientations of the specimen in the magnetic field. In general, image noise, subtle mis-registrations, or other artifacts also cause differences, given the complex, multistep QSM processing pipeline. Such noise contributions should be similar throughout the brain, while the observed differences show a clear anatomical pattern. The absolute difference between the reference χ_{33} and the estimated χ obtained in acquisitions at different specimen orientations was quantitatively examined in three selected WM ROIs (Fig. 6B). Among these regions, those with higher local anisotropy yielded greater differences upon reorienting the specimen, for example, between 0.01 and 0.08 ppm in the corpus callosum and internal capsule (mean values: 0.040 and 0.039, respectively) compared with values between 0.01 and 0.045 ppm in the centrum semiovale (mean: 0.022 ppm). The structural similarity index measure (SSIM) between χ_{33} and QSM at different orientations within the entire volume (Fig. 6C) fluctuated between 78% and 83% (mean: 81%, median: 81%). Additional voxel-wise mapping of the variance of differences between the STI-based χ_{33} reference and QSM estimates at different orientations also revealed increased variance in WM areas associated with higher anisotropy (Fig. 6D; red and blue arrows). Such variance variations were observed even within bundles. These resemble previously reported comparisons of QSM and STI-based reference results and highlight the need to account for orientation dependence in WM-χ estimates targeted at high accuracy.

3.4. ODF estimations

Characteristic examples of HARDI- and HARSI-derived ODFs with 4th-order spherical harmonics are shown in Fig. 7. Visual inspection indicates that diffusion-based ODFs point mostly towards one main fiber orientation while the phase-based ODFs show sensitivity to the secondary orientations, with the results indicating clearly separated lobes

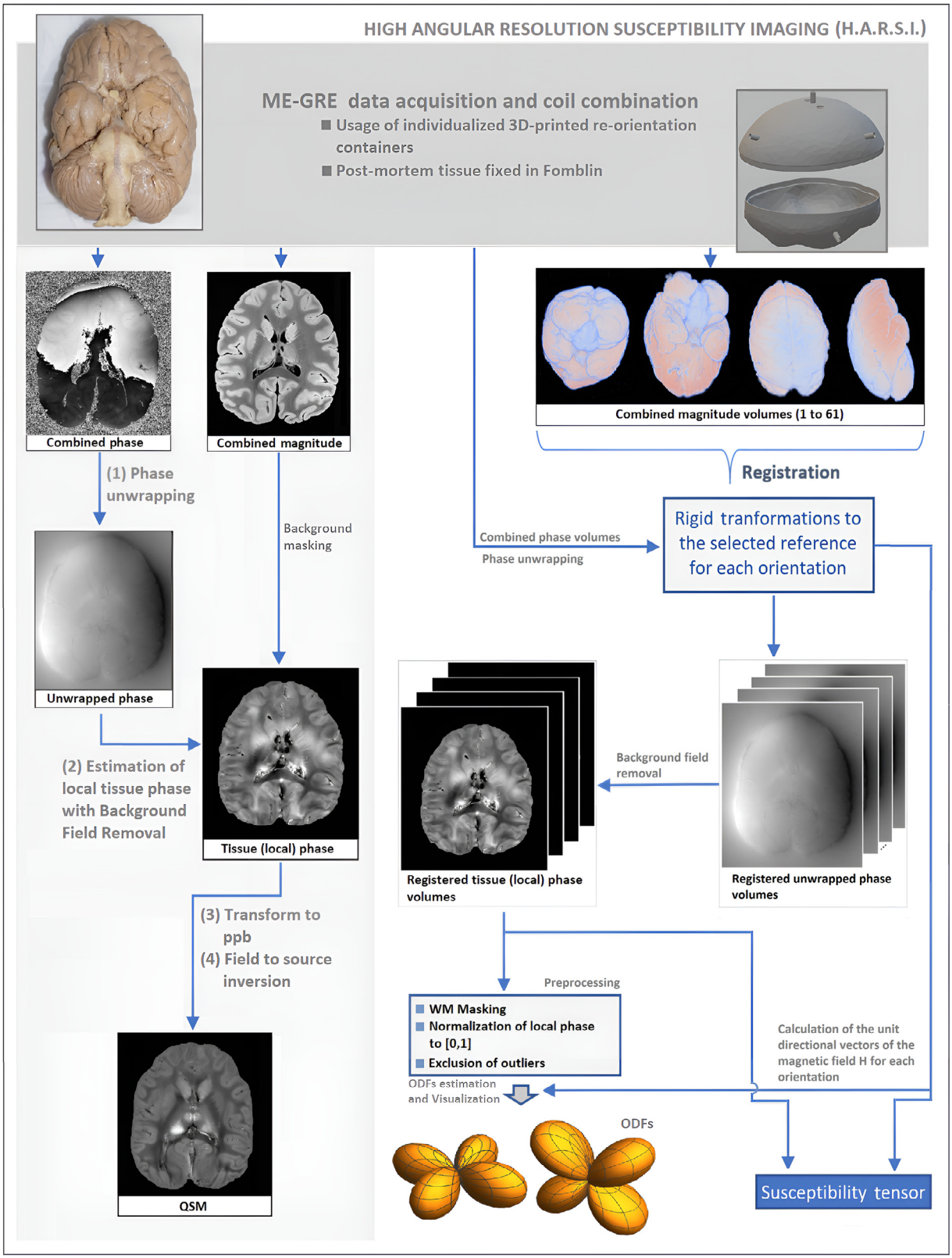

Fig. 2. Simplified schematics of the pipelines employed for QSM as well as STI and ODF derivation from high-angular GRE phase data. The complex-valued GRE data from each of the 32 coil channels are saved individually and combined using SVD-ESPIRiT. **(Left)** QSM pipeline starting with Laplacian phase unwrapping on the combined raw phase and local δB_0 estimation with background-field removal using V-SHARP and, finally, field-to-source inversion, to obtain relative χ values employing iLSQR. **(Right)** STI and HARSI pipeline with registration of the multi-orientation phase volumes to a reference employing transformations derived from registrations of the corresponding magnitude volumes. Phase unwrapping and background-field removal is performed individually for each orientation. iLSQR is also employed for susceptibility-tensor reconstruction. For ODF estimation, further pre-processing (masking, normalization, outlier removal) is required.

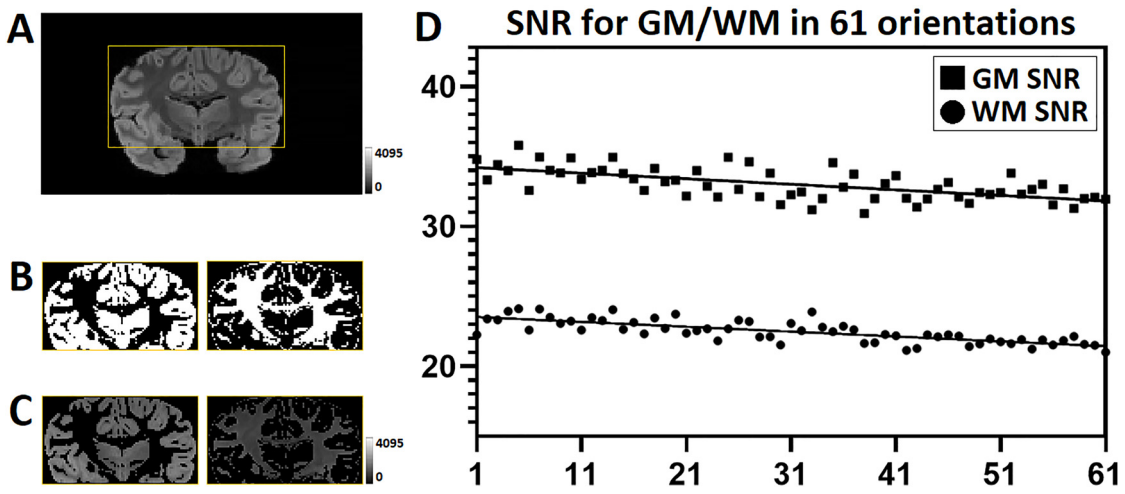

Fig. 3. **(A)** Indication of the ROI (central coronal slice) used for the SNR calculation of the magnitude GRE images and **(B)** GM and WM masks derived by thresholding of the reference image acquired at TE=29.48 ms as well as **(C)** corresponding (magnitude) signal intensities in these masks. **(D)** The SNR metrics obtained from the 61 registered, consecutively reoriented magnitude volumes shows minor fluctuations about the reference value in both WM (circles) and GM (squares) as well as a subtle drift. Note that the orientations in (D) are ordered according to the time of the individual acquisitions. The drifts can be fitted to straight lines, which were separately calculated for the WM and GM segments.

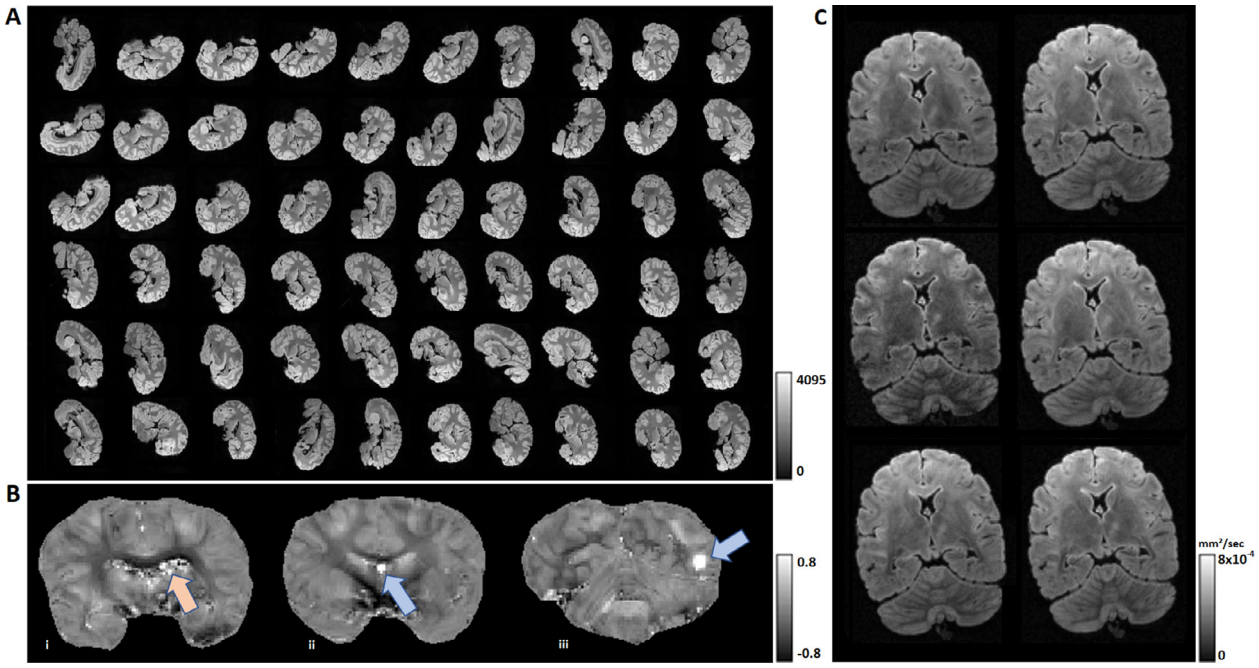

Fig. 4. **(A)** Demonstration of the magnitude image quality obtained at TE=29.48 ms in 61 consecutive GRE acquisitions with reorientation of the sample (center slice of each individual dataset). **(B)** Local phase images at the reference orientation indicating artifacts related to remaining small air bubbles within the cavity of the left lateral ventricle *(*left; orange arrow*)* as well as at two other positions (middle and right; blue arrows). **(C)** Examples of images obtained at different directions of the diffusion-weighting gradient for demonstration of the data quality of the DWI experiment.

of similar size, in at least two directions. To further evaluate this difference, the corpus callosum was selected as a region where fibers are mainly parallel to each other without many crossing fibers (Supplementary Figure S7). Consistently, the HARSI-based ODFs indicate strong orientational characteristics towards one dominating direction in this region, with subtle indications of secondary contributions. We cannot exclude that the latter contributions are due to artifacts resulting from strong susceptibility gradients induced by neighboring small bubbles and/or cavities impacting parts of the corpus callosum voxels (which would suggest with similar impacts in other voxels near interfaces) or from registration errors and numerical instabilities of the multi-step processing pipeline. Given the rather small deviation from an ODF of a single fiber population in these voxels, we assume that the observation of multiple ODF peaks with more prominent secondary contributions in other WM regions that are known to be impacted by fiber crossings may be indeed depicting underlying axonal characteristics.

Fig. 8A, demonstrates the effect from residual air bubbles in the left lateral ventricle leading to characteristic artifacts affecting the phase-based ODFs in the surrounding region. In comparison, diffusion-based ODFs appear to be more immune to such perturbations. Further exam-

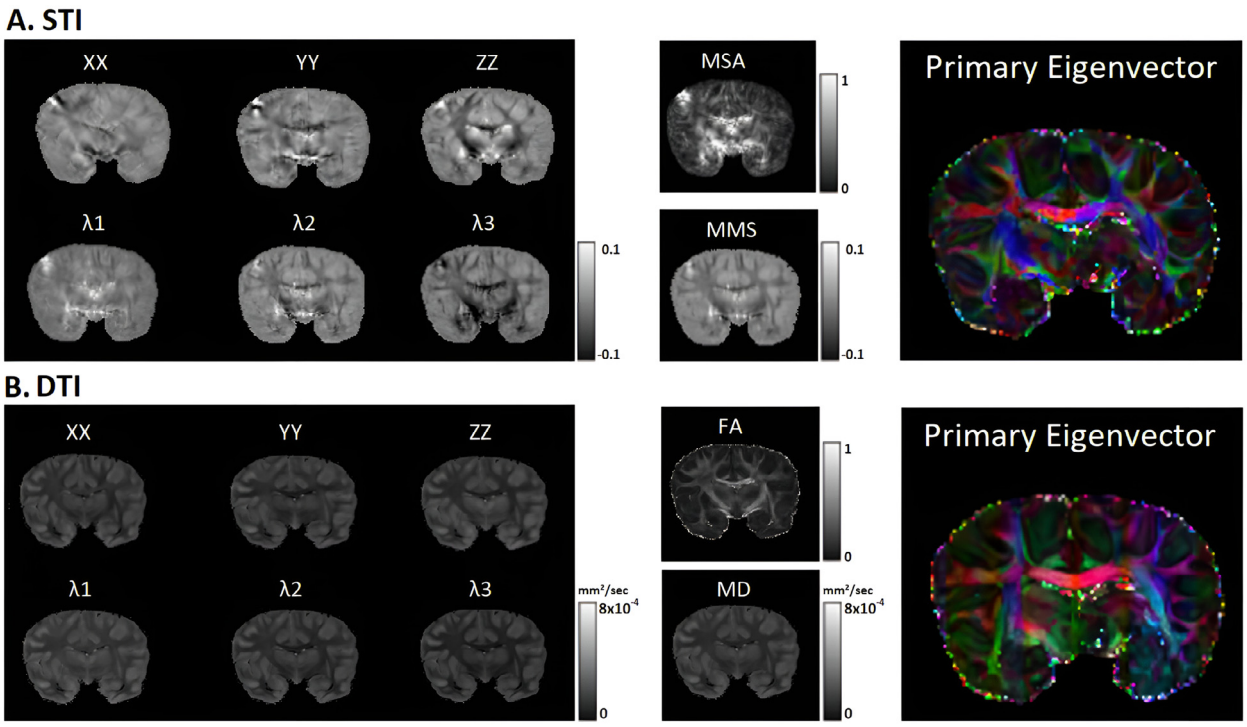

Fig. 5. **(A)** Diagonal susceptibility-tensor components obtained with STI (left column, top row) and corresponding eigenvalues (left column, bottom row) as well as MSA and MMS (middle column) and color-coded susceptibility primary eigenvector weighted by the DTI-based FA (right column). **(B)** Diagonal diffusion-tensor components obtained with DTI (left column, top row) and corresponding eigenvalues (left column, bottom row) as well as FA and MD (middle column) and color-coded also differences between the directions of the primary eigenvectors obtained with STI and DTI.

ples of ODFs obtained in artifact-free regions with diffusion and phase-based acquisitions are presented in Fig. 8B–D. These results indicate an efficiency in depicting characteristics of the underlying fiber formations for both methods as well as distinct differences in the local shapes of the spherical harmonics reflecting the distributions. Further evident is some additional noise in HARSI-derived ODFs, as expected due to the multistep processing pipeline required for susceptibility data including registration of the acquisitions at different orientation.

4. Discussion

The current work goes beyond earlier investigations of orientation dependence of magnetic susceptibility in the brain in several ways: *(i)* While previous experiments largely focused on fixed rodent brain, the chimpanzee brain is morphologically much closer to the human brain with similar cellular composition and relative volume of WM (Herculano-Houzel, 2012). However, the smaller size (approx. 400 g compared to a typical human brain of 1.5 kg) allows for unconstrained reorientation in a standard head coil and more efficient sampling supporting high angular and spatial resolution acquisitions within an acceptable time. *(ii)* With 61 orientations, the angular resolution matches current DWI protocols that support extraction of information on fiber orientation distributions to identify fiber crossings or other complex patterns in WM. This permits to go beyond previous work restricted to STI. *(iii)* Simultaneously acquired DWI data of the same angular and spatial resolution support direct voxel-level comparisons of phase and diffusion-based results.

Visual comparison of the ME acquisitions at different orientations to the reference scan indicate consistent quality, which is further supported by the comparison of the achieved image SNR. Apart from local artifacts due to a few remaining air bubbles, there were no extended susceptibility artifacts, while a high quality of the registration permitted voxel-wise analysis.

The HARSI-derived ODFs indicated sensitivity to complex geometries associated with intersecting axonal fiber bundles—similar to HARDI-derived results obtained at the same spatial and angular resolution. Interestingly, a closer qualitative voxel-wise comparison of estimated fiber densities suggests—in several instances—that HARSI-based results indicate separated lobes of similar size in two main directions, whereas HARDI-based ODFs appear to point more towards a main direction, with smaller sized lobes existing towards other directions. It is well documented that the water diffusion coefficient (at ambient temperature) is reduced to 30–50% of the *in-vivo* value (at body temperature) after *in-situ* perfusion fixation (Sun et al., 2003), with further alterations occurring during the *post-mortem* interval (i.e., the interval between death and fixation) (D'Arceuil & de Crespigny, 2007; Miller et al., 2011) and during fixation (Georgi et al., 2019; Yong-Hing et al., 2005). Diffusion anisotropy reductions in WM have also been observed (D'Arceuil & de Crespigny, 2007; Miller et al., 2011), which may be related to increased membrane permeability (Shepherd et al., 2009). Aldehyde fixation finally induces moderate (T_1) or strong (T_2) shortening of tissue water relaxation times (Pfefferbaum et al., 2004), which is, however, mitigated by soaking the specimen in PBS (Shepherd et al., 2009) as performed in the current study. Taken together, this leads to unfavorable conditions for high-resolution DWI as correspondingly stronger *b*-values are required for resolving multiple fiber populations, without excessive prolongation of TE. For *in-vivo* MRI of human brain, *b*-values around 3,000 s/mm^2 were recommended for an improved identification of peaks in the ODF (Jones et al, 2013). Considering the reduced diffusivity under conditions of the current work, the *b*-value of 5,000 s/mm^2 obtained at TE = 53.5 ms with the Connectom gradient system should suffice to resolve bundles intersecting at angles ≥45° but may fall short to robustly discriminate them in the range of 30–45° (Descoteaux et al., 2009). Consequently, the HARDI-based ODFs will be increasingly dominated by contributions from one major bundle for intersections at angles <45°

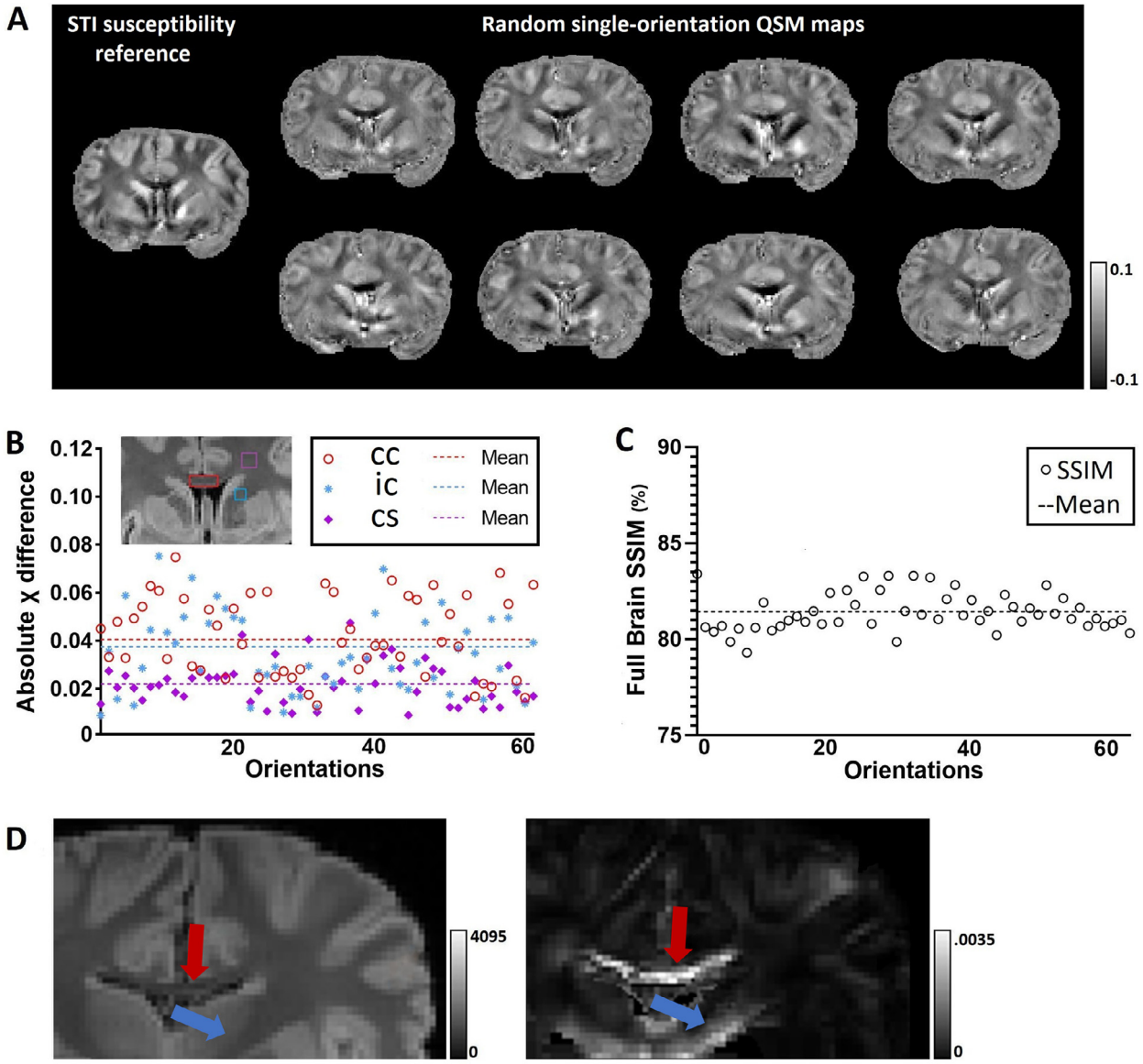

Fig. 6. QSM analyses performed under the assumption of a scalar susceptibility. **(A)** STI-based results taking the χ_{33} tensor component (Langkammer et al., 2018) as a reference susceptibility **(left)** and comparison with standard QSM results of eight (out of 61) exemplarily selected measurements with reorientation of the specimen in the magnetic field **(right). (B)** Absolute difference between the reference value χ_{33} (from STI) and QSM results obtained without consideration of orientation dependence in three selected WM ROIs. The numbering of different sample orientations is arbitrary following the order of the (randomized) acquisitions. Larger differences are obtained in areas of higher anisotropy e.g. corpus callosum (cc) and internal capsule (ic). The third region, centrum semiovale (cs) is indicating lower differences. **(C)** SSIM between the reference and QSM results without consideration of orientation dependence varies between 78 and 83%. **(D)** Voxel-wise variance map **(right)** of 61 QSM results obtained with different orientations. Similar to findings with DWI, increased variance is evident in areas of high structural anisotropy. The left image shows a magnitude image at the same slice position. Red and blue arrows indicate the corpus callosum and internal capsule, respectively.

For both HARDI- and HARSI-based ODF estimations, there is no immediate information about the relative position of different fiber populations within a given voxel, which limits the differentiation of 'crossing' and 'kissing' fiber configurations (Jones et al., 2013). Minimizing the number of voxels containing multiple bundles by increasing the spatial resolution is, therefore, of ongoing interest. Diffusion-based tractography in fixed mouse brain at (isotropic) 43 μm has been achieved in previous work employing a dedicated small-bore scanner (Calabrese et al., 2015). Scanning of hominid whole-brain specimens requires large magnet bores and is technically more challenging, but also particularly interesting due to their more complex WM architecture. Resolutions around 500 μm seem to be the current limit with available hardware in such experiments (Eichner et al., 2020; Fan et al., 2022). In comparison, QSM acquisitions are less demanding on the hardware, and the signal loss at TEs in the order of 25 ms at 3 T or 12 ms at 7 T that are required for sufficient phase evolution is smaller than that inherent to DWI. Consequently, human whole-brain (magnitude) GRE datasets at 100–200 μm are available as digital resources (Alkemade et al., 2022; Ding et al., 2016; Edlow et al., 2019). Although the precise registration of multi-orientation phase data remains challenging, the HARSI approach introduced here as a proof of concept holds great potential to go beyond current (spatial) resolution limits of diffusion-based investigations of connectivity patterns. Currently existing histological methodologies to obtain 3D information on the fiber architecture require complicated preparations (Morawski et al., 2018). These are important for a validation of MRI-derived results but currently limited to rather small brain sections.

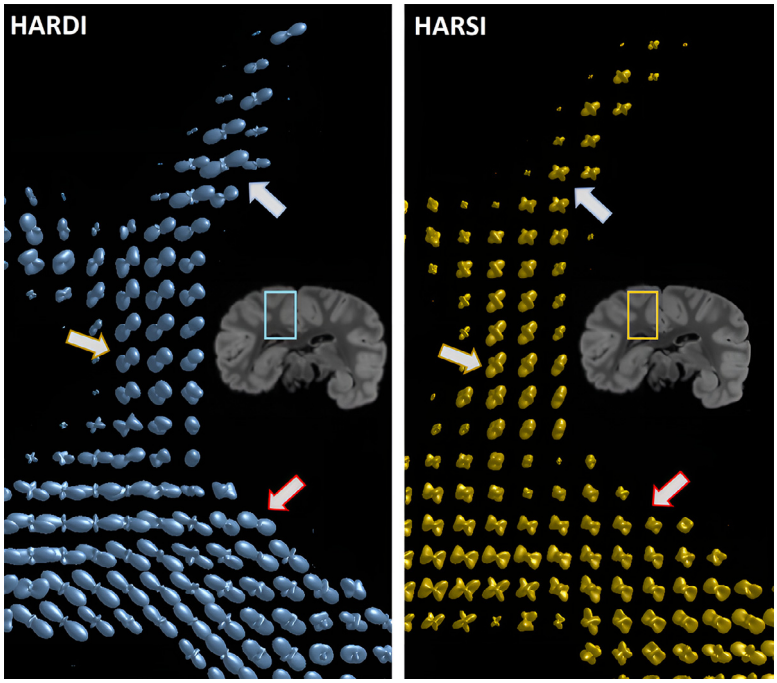

Fig. 7. Comparison of **(A)** HARDI and **(B)** HARSI-derived ODFs in a preselected ROI with WM and surrounding GM as indicated in the insert. Color-coding of directions is not shown to better emphasize on the directionality of the estimated spherical harmonics (4th order). Diffusion-based ODFs point mostly towards one main orientation. The phase-based ODFs suggest a different sensitivity to secondary fiber populations (see arrows pointing to characteristic examples). Further investigations are needed to validate this preliminary observation.

A fundamental difference between the HARSI approach in comparison to HARDI techniques lies in the biophysical underpinning of the contrast mechanism, which is unrelated to water diffusion. In WM, myelin is a major barrier to water diffusion and contributes to diffusion anisotropy, however, diffusion anisotropy is also observed when no myelin is present (Beaulieu, 2002; Sen & Basser, 2005). Myelin also provides a primary contribution to susceptibility, however, significant susceptibility anisotropy was not observed before myelination sets in (Argyridis et al., 2014). Moreover, the signal phase is also strongly affected by the presence of paramagnetic compounds, in particular, iron stores in oligodendrocytes and astrocytes (Möller et al., 2019). Glial cells are known to cluster in short rows parallel to the axons they support (Baumann & Pham-Dinh, 2001; Suzuki & Raisman, 1992), which has recently allowed to obtain information on WM fiber architecture from Nissl stainings of *post-mortem* histological slices (Schurr & Mezer, 2021). In summary, both contributions to susceptibility in WM are roughly characterized by cylindrical geometries (hollow cylinders and rows) and should, hence, report on the particular arrangement of fibers within a voxel. A fundamental difference, however, is that the diamagnetic contribution to (anisotropic) susceptibility from myelin results from components of anisotropic molecular structures in the lipid bilayers forming myelin (Wharton & Bowtell, 2012) whereas the paramagnetic contribution may be better described as a microscopic (i.e., cellular) compartmentalization of susceptibility sources (Chu et al., 1990; He & Yablonskiy, 2009; Lee et al., 2010).

A potential limitation of all susceptibility-based methods are strong susceptibility gradients, for example, at tissue boundaries (WM/GM boundary or WM/ventricle boundary) or around bubbles formed in *post-mortem* tissue. Such non-local magnetic fields affect neighboring regions, acting as small additional background fields, which may not be sufficiently captured by existing background-field removal methods (Deistung et al., 2017). In particular, the phase in these voxels may depend on the angle between the direction to a local boundary and the main magnetic field. Such inaccuracies in local phase images may impact the sensitivity and morphology of phase-based ODFs, which may be preferentially in the plane parallel to a boundary. Interestingly, because short association fibers run parallel to the WM/GM boundary, one would still expect good agreement with diffusion-based ODFs (as in our results), even if the phase-based ODFs are not driven by local fiber orientations. Field-to-source inversion should mitigate these effects, although, the susceptibility estimation may still be impacted in areas of strong perturbations. In our experiments, a comparison of the obtained orientation-dependent contrast variations in selected WM and GM voxels did not disclose systematic differences between the orientation dependencies of local tissue phase and bulk susceptibility (see Supplementary Figure S8), suggesting good agreement between both measures. Ultimately, ground-truth information about the local microstructure is required for a realistic assessing the accuracy of phase versus susceptibility-based (and also diffusion-based) ODFs. Such information may be obtained in small tissue sections with advanced 3D microscopy techniques (Morawski et al., 2018). Recent progress in modeling the Larmor frequency shift in terms of the underlying magnetic microstructure (Sandgaard et al., 2023) may further elucidate the impact from different susceptibility sources as well as non-local effects.

We note that the 12 echoes acquired for each orientation provide a potential for R_2^* reconstruction and further analyses related to tissue structure and composition, which is beyond the scope of this study. Recently, progress has been made in separating contributions to (isotropic) QSM from opposite susceptibility sources by modeling the R_2^* decay with multiple complex exponentials (Chen et al., 2021) or by considering different effects of susceptibility sources on the frequency shift and transverse relaxation rate (Shin et al., 2021). These techniques are, in general, compatible with our HARSI approach, and a corresponding combination might expand the information about microstructural tissue characteristics as well as molecular and microscopic sources of orientation dependence that are complementary to the information accessible through DWI.

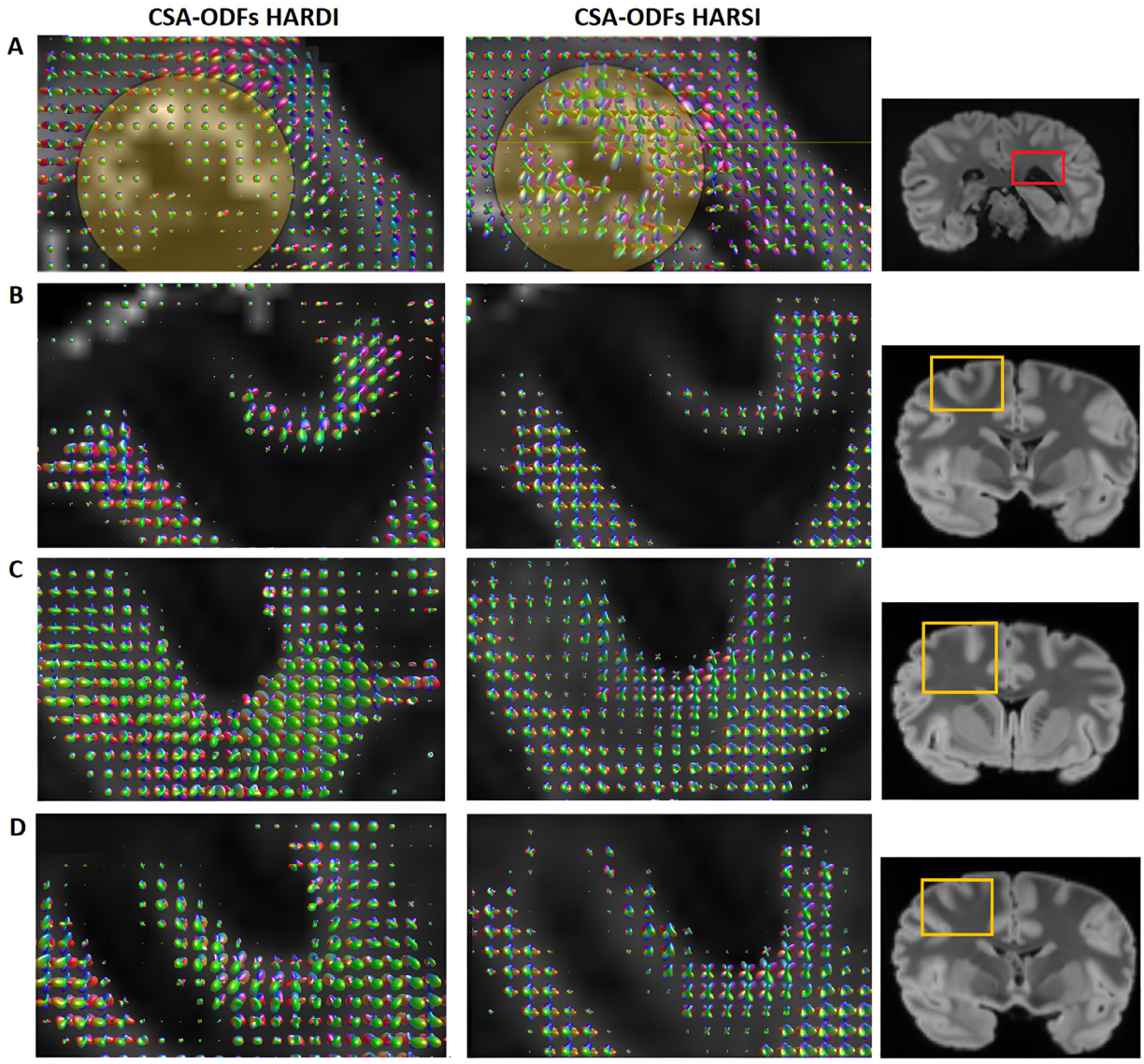

Fig. 8. CSA-ODFs (4th-order spherical harmonics; FA mask as background) in selected ROIs (indicated in the right column) obtained with HARSI (left column) and HARDI (central column). **(A)** Remaining air bubbles in the left ventricle produce local field distortions leading to characteristic perturbations of the phase-based ODFs in the surrounding region (circled area), whereas the diffusion-based ODFs are relatively immune to this artifact. **(B–D)** Resemblance between the methods as well as characteristic differences in the sensitivity to second-order fibers in regions that are free from such artifacts.

Declaration of Competing Interest

The authors declare no competing interest.

Credit authorship contribution statement

Dimitrios G. Gkotsoulias: Conceptualization, Methodology, Software, Validation, Formal analysis, Investigation, Writing – original draft, Writing – review & editing, Visualization. **Roland Müller:** Methodology, Resources. **Carsten Jäger:** Methodology, Resources. **Torsten Schlumm:** Software, Data curation. **Toralf Mildner:** Methodology, Resources, Writing – review & editing. **Cornelius Eichner:** Conceptualization, Writing – review & editing. **André Pampel:** Conceptualization, Writing – review & editing. **Jennifer Jaffe:** Resources. **Tobias Gräßle:** Resources. **Niklas Alsleben:** Software. **Jingjia Chen:** Validation. **Catherine Crockford:** Resources, Writing – review & editing. **Roman Wittig:** Resources, Writing – review & editing. **Chunlei Liu:** Conceptualization, Writing – review & editing, Funding acquisition. **Harald E. Möller:** Conceptualization, Methodology, Resources, Writing – original draft, Writing – review & editing, Supervision, Project administration, Funding acquisition.

Data availability

The dataset acquired and used within the scope of this study will be made publicly available, upon publication of the current work.

Acknowledgments

This work was funded by the EU through the ITN “INSPiRE-MED” (H2020-MSCA-ITN-2018, #813120). Chunlei Liu and Jingjia Chen were supported in part by the National Institute of Aging of the National Institutes of Health (Award No. R01AG070826). We particularly thank Angela D. Friederici and Nikolaus Weiskopf and further Evolution of Brain Connectivity (EBC) project organizers, the Ministère de l’Enseignement Supérieur et de la Recherche Scientifique and the Ministère des Eaux et Fôrets, Côte d’Ivoire, the Office Ivoirien des Parcs et Réserves, and the staff of the Taï Chimpanzee Project for permitting and supporting this

research. Appreciation is extended to Michael Paquette, Riccardo Metere and Alfred Anwander for helpful methodological discussions and sharing of related processing packages.

Supplementary materials

Supplementary material associated with this article can be found, in the online version, at doi:10.1016/j.neuroimage.2023.120202.

References

Alkemade, A., Bazin, P.-L., Balesar, R., Pine, K., Kirilina, E., Möller, H.E., Trampel, R., Kros, J.M., Keuken, M.C., Bleys, R.L.A.W., Swaab, D.F., Herrler, A., Weiskopf, N., Forstmann, B.U., 2022. A unified 3D map of microscopic architecture and MRI of the human brain. Sci. Adv. 8 (17), eabj7892. doi:10.1126/sciadv.abj7892.

Alkemade, A., Pine, K., Kirilina, E., Keuken, M.C., Mulder, M.J., Balesar, R., Groot, J.M., Bleys, R.L.A.W., Trampel, R., Weiskopf, N., Herrler, A., Möller, H.E., Bazin, P.-L., Forstmann, B.U., 2020. 7 Tesla MRI followed by histological 3D reconstructions in whole-brain specimens. Front. Neuroanat. 14, 536838. doi:10.3389/fnana.2020.536838.

Argyridis, I., Li, W., Johnson, G.A., Liu, C., 2014. Quantitative magnetic susceptibility of the developing mouse brain reveals microstructural changes in the white matter. NeuroImage 88, 134–142. doi:10.1016/j.neuroimage.2013.11.026.

Basser, P.J., Mattiello, J., LeBihan, D., 1994a. Estimation of the effective self-diffusion tensor from the NMR spin echo. J. Magn. Reson. B 103 (3), 247–254. doi:10.1006/jmrb.1994.1037.

Basser, P.J., Mattiello, J., LeBihan, D., 1994b. MR diffusion *tensor* spectroscopy and imaging. Biophys. J. 66 (1), 259–267. doi:10.1016/S0006-3495(94)80775-1.

Baumann, N., Pham-Dinh, D., 2001. Biology of oligodendrocyte and myelin in the mammalian central nervous system. Physiol. Rev. 81 (3), 871–927. doi:10.1152/physrev.2001.81.2.871.

Beaulieu, C., 2002. The basis of anisotropic water diffusion in the nervous system – a technical review. NMR Biomed 15 (7-8), 435–455. doi:10.1002/nbm.782.

Benveniste, H., Einstein, G., Kim, K.R., Hulette, C., Johnson, G.A., 1999. Detection of neuritic plaques in Alzheimer's disease by magnetic resonance microscopy. Proc. Natl. Acad. Sci. USA 96 (24), 14079–14084. doi:10.1073/pnas.96.24.14079.

Bilgic, B., Polimeni, J.R., Wald, L.L., Setsompop, K., 2016a. Automated tissue phase and QSM estimation from multichannel data. In: Proceedings of the 24th Annual Meeting of ISMRM, Singapore, p. 2849.

Bilgic, B., Xie, L., Dibb, R., Langkammer, C., Mutluay, A., Ye, H., Polimeni, J.R., Augustinack, J., Liu, C., Wald, L.L., Setsompop, K., 2016b. Rapid multi-orientation quantitative susceptibility mapping. NeuroImage 125, 1131–1141. doi:10.1016/j.neuroimage.2015.08.015.

Birkl, C., Langkammer, C., Krenn, H., Goessler, W., Ernst, C., Haybaeck, J., Stollberger, R., Fazekas, F., Ropele, S., 2015. Iron mapping using the temperature dependency of the magnetic susceptibility. Magn. Reson. Med. 73 (3), 1282–1288. doi:10.1002/mrm.25236.

Calabrese, E., Badea, A., Cofer, G., Qi, Y., Johnson, G.A., 2015. A diffusion MRI tractography connectome of the mouse brain and comparison with neuronal tracer data. Cereb. Cortex 25 (11), 4628–4637. doi:10.1093/cercor/bhv121.

Chen, J., Gong, N.-J., Chaim, K.T., Otaduy, M.C.G., Liu, C., 2021. Decompose quantitative susceptibility mapping (QSM) to sub-voxel diamagnetic and paramagnetic components based on gradient-echo MRI data. NeuroImage 242, 118477. doi:10.1016/j.neuroimage.2021.118477.

Chu, S.C.-K, Xu, Y., Balschi, J.A., Springer Jr., C.S., 1990. Bulk magnetic susceptibility shifts in NMR studies of compartmentalized samples: Use of paramagnetic reagents. Magn. Reson. Med. 13 (2), 239–262. doi:10.1002/mrm.1910130207.

D'Arceuil, H., de Crespigny, A., 2007. The effects of brain tissue decomposition on diffusion tensor imaging and tractography. NeuroImage 36 (1), 64–68. doi:10.1016/j.neuroimage.2007.02.039.

Deistung, A., Schweser, F., Reichenbach, J.R., 2017. Overview of quantitative susceptibility mapping. NMR Biomed. 30 (4), e3569. doi:10.1002/nbm.3569.

de Rochefort, L., Liu, T., Kressler, B., Liu, J., Spincemaille, P., Lebon, V., Wu, J., Yi Wang, Y., 2010. Quantitative susceptibility map reconstruction from MR phase data using Bayesian regularization: validation and application to brain imaging. Magn. Reson. Med. 63 (1), 194–206. doi:10.1002/mrm.22187.

Descoteaux, M., Deriche, R., Knösche, T.R., Anwander, A., 2009. Deterministic and probabilistic tractography based on complex fibre orientation distributions. IEEE Trans. Med. Imaging 28 (2), 269–286. doi:10.1109/TMI.2008.2004424.

Ding, S.-L., Royall, J.J., Sunkin, S.M., Ng, L., Facer, B.A.C., Lesnar, P., Guillozet-Bongaarts, A., McMurray, B., Szafer, A., Dolbeare, T.A., Stevens, A., Tirrell, L., Benner, T., Caldejon, S., Dalley, R.A., Dee, N., Lau, C., Nyhus, J., Reding, M., Riley, Z.L., Sandman, D., Shen, E., van der Kouwe, A., Varjabedian, A., Write, M., Zollei, L., Dang, C., Knowles, J.A., Koch, C., Phillips, J.W., Sestan, N., Wohnoutka, P., Zielke, H.R., Hohmann, J.G., Jones, A.R., Bernard, A., Hawrylycz, M.J., Hof, P.R., Fischl, B., Lein, E.S., 2016. Comprehensive cellular-resolution atlas of the adult human brain. J. Comp. Neurol. 524 (16), 3127–3481. doi:10.1002/cne.24080.

Edlow, B.L., Mareyam, A., Horn, A., Polimeni, J.R., Witzel, T., Tisdall, M.D., Augustiniak, J.C., Stockmann, J.P., Diamond, B.R., Stevens, A., Tirrell, L.E., Folkerth, R.D., Wald, L.L., Fischl, B., van der Kouwe, A., 2019. 7 Tesla MRI of the ex vivo human brain at 100 μm resolution. Sci. Data 6, 244. doi:10.1038/s41597-019-0254-8.

Eichner, C., Paquette, M., Mildner, T., Schlumm, T., Pléh, K., Samuni, L., Crockford, C., Wittig, R.M., Jäger, C., Möller, H.E., Friederici, A.D., Anwander, A., 2020. Increased sensitivity and signal-to-noise ratio in diffusion-weighted MRI using multi-echo acquisitions. NeuroImage 221, 117172. doi:10.1016/j.neuroimage.2020.117172.

Fan, Q., Eichner, C., Afzali, M., Mueller, L., Tax, C.M.W., Davids, M., Mahmutovic, M., Keil, B., Bilgic, B., Setsompop, K., Lee, H.-H., Tian, Q., Chiara Maffei, C., Ramos-Llordén, G., Nummenmaa, A., Witzel, T., Yendiki, A., Song, Y.-Q., Huang, C.-C., Lin, C.-P., Weiskopf, N., Anwander, A., Jones, D.K., Rosen, B.R., Wald, L.L., Huang, S.Y., 2022. Mapping the human connectome using diffusion MRI at 300 mT/m gradient strength: Methodological advances and scientific impact. NeuroImage 254, 118958. doi:10.1016/j.neuroimage.2022.118958.

Feinberg, D.A., Hale, J.D., Watts, J.C., Kaufman, L., Mark, A., 1986. Halving MR imaging time by conjugation: Demonstration at 3.5 kG. Radiology 161 (2), 527–531. doi:10.1148/radiology.161.2.3763926.

Frahm, J., Haase, A., Matthaei, D., 1986. Rapid three-dimensional MR imaging using the FLASH technique. J. Comput. Assist. Tomogr. 10 (2), 363–368. doi:10.1097/00004728-198603000-00046.

Frank, L.R., 2001. Anisotropy in high angular resolution diffusion-weighted MRI. Magn. Reson. Med. 45 (6), 935–939.

Georgi, J., Metere, R., Jäger, C., Möller, H.E., 2019. Influence of the extracellular matrix on water mobility in subcortical gray matter. Magn. Reson. Med. 81 (2), 1265–1279. doi:10.1002/mrm.27459.

Griswold, M.A., Jakob, P.M., Heidemann, R.M., Nittka, M., Jellus, V., Wang, J., Kiefer, B., Haase, A., 2002. Generalized autocalibrating partially parallel acquisitions (GRAPPA). Magn. Reson. Med. 47 (6), 1202–1210. doi:10.1002/mrm.10171.

He, X., Yablonskiy, D.A., 2009. Biophysical mechanisms of phase contrast in gradient echo MRI. Proc. Natl. Acad. Sci. USA 106 (32), 13558–13563. doi:10.1073/pnas.0904899106.

Herculano-Houzel, S., 2012. The remarkable, yet not extraordinary, human brain as a scaled-up primate brain and its associated cost. Proc. Natl. Acad. Sci. USA 109 (1), 10661–10668. doi:10.1073/pnas.1201895109, suppl.

Jenkinson, M., Beckmann, C.F., Behrens, T.E., Woolrich, M.W., Smith, S.M., 2012. FSL. NeuroImage 62 (2), 782–790. doi:10.1016/j.neuroimage.2011.09.015.

Jones, D.K., Knösche, T.R., Turner, R., 2013. White matter integrity, fiber count, and other fallacies: the do's and don'ts of diffusion MRI. NeuroImage 73, 239–254. doi:10.1016/j.neuroimage.2012.06.081.

Jones, D.K., Horsfield, M.A., Simmons, A., 1999. Optimal strategies for measuring diffusion in anisotropic systems by magnetic resonance imaging. Magn. Reson. Med. 42 (3), 515–525. doi:10.1002/(SICI)1522-2594(199909)42:3<515::AID-MRM14>3.0.CO;2-Q.

Kamath, A., Aganj, I., Xu, J., Yacoub, E., Ugurbil, K., Sapiro, G., Lenglet, C. 2012. Generalized constant solid angle ODF and optimal acquisition protocol for fiber orientation mapping. In: Proceedings of the MICCAI 2012 Workshop on Computational Diffusion MRI, Nice, France, pp. 67–78.

Labadie, C., Hetzer, S., Schulz, J., Mildner, T., Aubert-Frécon, M., Möller, H.E., 2013. Center-out echo-planar spectroscopic imaging with correction of gradient-echo phase and time shifts. Magn. Reson. Med. 70 (1), 16–24. doi:10.1002/mrm.24428.

Langkammer, C., Schweser, F., Shmueli, K., Kames, C., Li, X., Guo, L., Milovic, C., Kim, J., Wei, H., Bredies, K., Buch, S., Guo, Y., Liu, Z., Meineke, J., Rauscher, A., Marques, J.P., Bilgic, B., 2018. Quantitative susceptibility mapping: Report from the 2016 reconstruction challenge. Magn. Reson. Med. 79 (3), 1661–1673. doi:10.1002/mrm.26830.

Lee, J., Shmueli, K., Fukunaga, M., van Gelderen, P., Merkle, H., Silva, A.C., Duyn, J.H., 2010. Sensitivity of MRI resonance frequency to the orientation of brain tissue microstructure. Proc. Natl. Acad. Sci. USA 107 (11), 5130–5135. doi:10.1073/pnas.0910222107.

Li, W., Wu, B., Liu, C., 2014. STI Suite: A software package for quantitative susceptibility imaging. In: Proceedings of the 23rd Annual Meeting of ISMRM, Milan, Italy, p. 3265.

Li, W., Liu, C., Duong, T.Q., van Zijl, P.C.M., Li, X., 2017. Susceptibility tensor imaging (STI) of the brain. NMR Biomed. 30 (4), e3540. doi:10.1002/nbm.3540.

Li, W., Wu, B., Liu, C., 2011. Quantitative susceptibility mapping of human brain reflects spatial variation in tissue composition. NeuroImage 55 (4), 1645–1656. doi:10.1016/j.neuroimage.2010.11.088.

Li, W., Wang, N., Yu, F., Han, H., Cao, W., Romero, R., Tantiwongkosi, B., Duong, T.Q., Liu, C., 2015. A method for estimating and removing streaking artifacts in quantitative susceptibility mapping. NeuroImage 108, 111–122. doi:10.1016/j.neuroimage.2014.12.043.

Li, W., Wu, B., Avram, A.V., Liu, C., 2012a. Magnetic susceptibility anisotropy of human brain in vivo and its molecular underpinnings. NeuroImage 59 (3), 2088–2097. doi:10.1016/j.neuroimage.2011.10.038.

Li, X., Vikram, D.S., Lim, I.A., Jones, C.K., Farrell, J.A., van Zijl, P.C., 2012b. Mapping magnetic susceptibility anisotropies of white matter in vivo in the human brain at 7 T. NeuroImage 62 (1), 314–330. doi:10.1016/j.neuroimage.2012.04.042.

Liu, C., 2010. Susceptibility tensor imaging. Magn. Reson. Med. 63 (6), 1471–1477. doi:10.1002/mrm.22482.

Liu, C., Li, W., Tong, K.A., Yeom, K.W., Kuzminski, S., 2015. Susceptibility-weighted imaging and quantitative susceptibility mapping in the brain. J. Magn. Reson. Imaging 42 (1), 23–41. doi:10.1002/jmri.24768.

Liu, C., Li, W., Wu, B., Jiang, Y., Johnson, G.A., 2012. 3D fiber tractography with susceptibility tensor imaging. NeuroImage 59 (2), 1290–1298. doi:10.1016/j.neuroimage.2011.07.096.

Liu, C., Murphy, N.E., Li, W., 2013. Probing white-matter microstructure with higher-order diffusion tensors and susceptibility tensor MRI. Front. Integr. Neurosci. 7, 11. doi:10.3389/fnint.2013.00011.

Marschner, H., Pampel, A., Müller, R., Reimann, K., Bock, N., Morawski, M., Geyer, S., Möller, H.E., 2023. High-resolution magnetization transfer imaging of *post-mortem*

marmoset brain: comparisons with relaxometry and histology. NeuroImage 268, 119860. doi:10.1016/j.neuroimage.2023.119860.

Metere, R., Möller, H.E., 2017. PyMRT and DCMPI: two new Python packages for MRI data analysis. In: Proceedings of the 25th Annual Meeting of ISMRM. Honolulu, HI, USA, p. 3816.

Miller, K.L., Stagg, C.J., Douaud, G., Jbabdi, S., Smith, S.M., Behrens, T.E.J., Jenkinson, M., Chance, S.A., Esiri, M.M., Voets, N.L., Jenkinson, N., Aziz, T.Z., Turner, M.R., Johansen-Berg, H., McNab, J.A., 2011. Diffusion imaging of whole, post-mortem human brains on a clinical MRI scanner. NeuroImage 57 (1), 167–181. doi:10.1016/j.neuroimage.2011.03.070.

Milovic, C., Tejos, C., Acosta-Cabronero, J., Özbay, P.S., Schwesser, F., Marques, J.P., Irarrazaval, P., Bilgic, B., Langkammer, C., 2020. The 2016 QSM Challenge: Lessons learned and considerations for a future challenge design. Magn. Reson. Med. 84 (3), 1624–1637. doi:10.1002/mrm.28185.

Möller, H.E., Bossoni, L., Connor, J.R., Crichton, R.R., Does, M.D., Ward, R.J., Zecca, L., Zucca, F.A., Ronen, I., 2019. Iron, myelin, and the brain: Neuroimaging meets neurobiology. Trend. Neurosci. 42 (6), 384–401. doi:10.1016/j.tins.2019.03.009.

Morawski, M., Kirilina, E., Scherf, N., Jäger, C., Reimann, K., Trampel, R., Gavriilidis, F., Geyer, S., Biedermann, B., Arendt, T., Weiskopf, N., 2018. Developing 3D microscopy with CLARITY on human brain tissue: towards a tool for informing and validating MRI-based histology. NeuroImage 182, 417–428. doi:10.1016/j.neuroimage.2017.11.060.

Novikov, D.S., Kiselev, V.G., Jespersen, S.N., 2018. On modeling. Magn. Reson. Med. 79 (6), 3172–3193. doi:10.1002/mrm.27101.

Özbay, P.S., Deistung, A., Feng, X., Nanz, D., Reichenbach, J.R., Schweser, F., 2017. A comprehensive numerical analysis of background phase correction with V-SHARP. NMR Biomed. 30 (4), e3550. doi:10.1002/nbm.3550.

Pfefferbaum, A., Sullivan, E.V., Adalsteinsson, E., Garrick, T., Harper, C., 2004. Postmortem MR imaging of formalin-fixed human brain. NeuroImage 21 (4), 1585–1595. doi:10.1016/j.neuroimage.2003.11.024.

Robinson, S.D., Bredies, K., Khabipova, D., Dymerska, B., Marques, J.P., Schweser, F., 2017. An illustrated comparison of processing methods for MR phase imaging and QSM: Combining array coil signals and phase unwrapping. NMR Biomed. 30 (4), e3601. doi:10.1002/nbm.3601.

Sandgaard, A.D., Shemesh, N., Kiselev, V.G., Jespersen, S.N., 2023. Larmor frequency shift from magnetized cylinders with arbitrary orientation distribution. NMR Biomed. 36 (3), e4859. doi:10.1002/nbm.4859.

Schäfer, A., Wharton, S., Gowland, P., Bowtell, R., 2009. Using magnetic field simulation to study susceptibility-related phase contrast in gradient echo MRI. NeuroImage 48 (1), 126–137. doi:10.1016/j.neuroimage.2009.05.093.

Schofield, M.A., Zhu, Y., 2003. Fast phase unwrapping algorithm for interferometric applications. Opt. Lett. 28 (14), 1194–1196. doi:10.1364/OL.28.001194.

Schurr, R., Mezer, A.A., 2021. The glial framework reveals white matter fiber architecture in human and primate brains. Science 374 (6568), 762–767. doi:10.1126/science.abj7960.

Schweser, F., Deistung, A., Lehr, B.W., Reichenbach, J.R., 2011. Quantitative imaging of intrinsic magnetic tissue properties using MRI signal phase: An approach to in vivo brain iron metabolism? NeuroImage 54 (4), 2789–2807. doi:10.1016/j.neuroimage.2010.10.070.

Schweser, F., Robinson, S.D., de Rochefort, L., Lie, W., Bredies, K., 2017. An illustrated comparison of processing methods for phase MRI and QSM: removal of background field contributions from sources outside the region of interest. NMR Biomed. 30 (4), e3604. doi:10.1002/nbm.3604.

Sen, P.N., Basser, P.J., 2005. A model for diffusion in white matter in the brain. Biophys. J. 89 (5), 2927–2938. doi:10.1529/biophysj.105.063016.

Shepherd, T.M., Thelwall, P.E., Stanisz, G.J., Blackband, S.J., 2009. Aldehyde fixative solutions alter the water relaxation and diffusion properties of nervous tissue. Magn. Reson. Med. 62 (1), 26–34. doi:10.1002/mrm.21977.

Shi, Y., Cao, S., Li, X., Feng, R., Zhuang, J., Zhang, Y., Liu, C., Wie, H., 2022. Regularized asymmetric susceptibility tensor imaging in the human brain in vivo. IEEE J. Biomed. Health Inform. 26 (9), 4508–4518. doi:10.1109/JBHI.2022.3182969.

Shin, H.-G., Lee, J., Yun, Y.H., Yoo, S.H., Jang, J., Oh, S.-H., Nam, Y., Jung, S., Kim, S., Fukunaga, M., Kim, W., Choi, H.J., Lee, J., 2021. χ-separation: Magnetic susceptibility source separation towerd iron and myelin mapping in the brain. NeuroImage 240, 118371. doi:10.1016/j.neuroimage.2021.118371.

Shmueli, K., de Zwart, J.A., van Gelderen, P., Li, T.-Q., Dodd, S.J., Duyn, J.H., 2009. Magnetic susceptibility mapping of brain tissue in vivo using MRI phase data. Magn. Reson. Med. 62 (4), 1510–1522. doi:10.1002/mrm.22135.

Sun, S.-W., Neil, J.J., Song, S.-K., 2003. Relative indices of water diffusion anisotropy are equivalent in live and formalin-fixed mouse brains. Magn. Reson. Med. 50 (4), 743–748. doi:10.1002/mrm.10605.

Suzuki, M, Rainman, G., 1992. The glial framework of central white matter tracts: Segmented rows of contiguous interfascicular oligodendrocytes and solitary astrocytes give rise to a continuous meshwork of transverse and longitudinal processes in the adult rat fimbria. Glia 6 (3), 222–235. doi:10.1002/glia.440060310.

Tournier, J.-D., Calamante, F., Gadian, D.G., Connelly, A., 2004. Direct estimation of the fiber orientation density function from diffusion-weighted MRI data using spherical deconvolution. NeuroImage 23 (3), 1176–1185. doi:10.1016/j.neuroimage.2004.07.037.

Tournier, J.-D., Smith, R., Raffelt, D., Tabbara, R., Dhollander, T., Pietsch, M., Christiaens, D., Jeurissen, B., Yeh, C.-H., Connelly, A., 2019. *MRtrix3*: a fast, flexible and open software framework for medical image processing and visualisation. NeuroImage 202, 116137. doi:10.1016/j.neuroimage.2019.116137.

Tuch, D.S., Reese, T.G., Wiegell, M.R., Makris, N., Belliveau, J.W., Wedeen, V.J., 2002. High angular resolution diffusion imaging reveals intravoxel white matter fiber heterogeneity. Magn. Reson. Med. 48 (6), 577–582. doi:10.1002/mrm.10268.

Tuch, D.S., Weisskoff, R.M., Belliveau, J.W., Wedeen, V.J., 1999. High angular resolution diffusion imaging of the human brain. In: Proceedings of the 7th Annual Meeting of ISMRM, Philadelphia, PA, USA, 1999, p. 321.

Uecker, M., Holme, C., Blumenthal, M., Wang, X., Tan, Z., Scholand, N., Iyer, S., Tamir, J., Lustig, M., 2021. mrirecon/bart: version 0.7.00. Zenodo doi: 10.5281/zenodo.4570601.

Uecker, M., Lustig, M., 2017. Estimating absolute-phase maps using ESPIRiT and virtual conjugate coils. Magn. Reson. Med. 77 (3), 1201–1207. doi:10.1002/mrm.26191.

Wharton, S., Bowtell, R., 2012. Fiber orientation-dependent white matter contrast in gradient echo MRI. Proc. Natl. Acad. Sci. USA 109 (45), 18559–18564. doi:10.1073/pnas.1211075109.

Wu, B., Li, W., Avram, A.V., Gho, S.-M., Liu, C., 2012. Fast and tissue-optimized mapping of magnetic susceptibility and T2* with multi-echo and multi-shot spirals. NeuroImage 59 (1), 297–305. doi:10.1016/j.neuroimage.2011.07.019.

Yong-Hing, C.J., Obenaus, A., Stryker, R., Tong, K., Sarty, G.E., 2005. Magnetic resonance imaging and mathematical modeling of progressive formalin fixation of the human brain. Magn. Reson. Med. 54 (2), 324–332. doi:10.1002/mrm.20578.